Interfacial Coexistence of Superconductivity and Magnetism in NbN/$MnBi_2Te_4$ Heterostructures

Yanjiang Wang Peng Dong Xiaohui Zeng Chen Xu Jianjun Xiao Chenyazhi Hu Yang Zhao Jinghui Wang Yueshen Wu Xiang Zhou Yanfeng Guo Yulin Chen Thorsten Hesjedal* Jun Li**

Y. Wang and P. Dong contributed equally to this work.

Emails: zhouxiang@shanghaitech.edu.cn, Thorsten.Hesjedal@physics.ox.ac.uk, lijun3@shanghaitech.edu.cn

Y. Wang, P. Dong, C. Xu, X. Zeng, J. Xiao, C. Hu, J. Wang, Y. Wu, X. Zhou, Y. Guo, Y. Chen, J. Li
School of Physical Science and Technology, ShanghaiTech University, Shanghai 201210, China
State Key Laboratory of Quantum Functional Materials, ShanghaiTech University, Shanghai 201210, China

J. Wang, X. Zhou, Y. Guo, Y. Chen, J. Li
ShanghaiTech Laboratory for Topological Physics, ShanghaiTech University, Shanghai 201210, China

Y. Chen, T. Hesjedal
Department of Physics, Clarendon Laboratory, University of Oxford, Oxford OX1 3PU, United Kingdom

Magnetic/superconducting thin-film heterostructures represent a frontier in condensed matter physics, offering pathways to realize unconventional pairing mechanisms such as topological superconductivity, spin-triplet pairing, and Majorana zero modes for fault-tolerant quantum computing. In this work, we integrate the magnetic van der Waals material $MnBi_2Te_4$ with a superconducting NbN thin film, achieving ultralow-disorder interfaces through Ti buffer layer engineering. Out-of-plane magnetoresistance hysteresis loops confirm interfacial spin polarization. Temperature- and field-dependent critical currents, extracted from differential resistance spectra, reveal robust coupling between the $MnBi_2Te_4$ surface states and the superconducting order of NbN, enabling proximity-induced superconductivity within $MnBi_2Te_4$. Notably, the proximity-induced critical currents remain invariant under in-plane field rotation, in contrast to the anisotropic response observed in bare NbN. These findings demonstrate a novel platform for fabricating high-quality heterointerfaces and enable targeted exploration of exotic quantum states.

1 Introduction

The interplay between magnetism and superconductivity has intrigued the condensed matter physics community for nearly a century [1, 2, 3, 4, 5]. Conventionally, these two phenomena are considered to be mutually exclusive, as magnetic ordering tends to disrupt the spin-singlet Cooper pairs responsible for conventional superconductivity [1]. However, the discovery of unconventional superconductors, including cuprates, heavy fermion compounds, and iron-based superconductors, has challenged this perspective. In these systems, superconductivity is often mediated by spin fluctuations rather than phonons [6, 7, 8, 9]. This has spurred a growing interest in identifying materials and systems where magnetism and superconductivity coexist, particularly in strongly correlated or high-temperature superconductors such as UGe_2 [10, 11], UTe_2 [12, 13], and Fe(Te,Se) [14]. In parallel, magnetic/superconducting heterostructures have emerged as ideal platforms for studying the coexistence of these competing orders. At their interfaces, proximity effects can give rise to hybrid superconducting-magnetic states [15, 16, 17, 18, 19]. Over the past decade, such heterostructures have gained importance in the context of superconducting quantum computing [20, 21, 22], following the theoretical proposal by Fu and Kane that proximity-induced topological superconductivity could host Majorana zero modes [23]. While proximity effects offer a promising route to realizing exotic quantum states, prior efforts have largely focused on bulk systems to minimize the influence of interfacial disorder, which can obscure or even dominate the intrinsic physics [24, 25]. In contrast, high-quality magnetic/superconducting interfaces are now being actively pursued to provide clean and controllable platforms for probing fundamental quantum phenomena.

Recently, $MnBi_2Te_4$ (MBT) has emerged as a key material in the study of topological magnetism. It is an intrinsic topological insulator with an ABC-stacked van der Waals crystal structure and A-type antiferromagnetic order [26, 27, 28, 29, 30]. In odd-layer MBT flakes, quantum anomalous Hall and Chern insulator states have been experimentally observed, while even-layer devices exhibit exotic phenomena such as the layer Hall effect and axion quasiparticles [26, 28, 31]. Theoretical proposals have further suggested that heterostructures combining MBT with conventional *s*-wave superconductors could host chiral Majorana edge modes [23, 32, 33]. Experimentally, Nb and NbN thin films have been deposited on MBT substrates [34, 35], and a proximity-induced superconducting gap of ≈0.1 meV has been observed. However, the nature of the interfacial magnetic state remains ambiguous, possibly due to the the fact that the superconducting layers have been directly deposited onto MBT using high-power sputtering which is known to lead to interface degradation of van der Waals materials. More recent studies using van der Waals heterostructures, such as $NbSe_2$/MBT, have revealed signatures of ferromagnetic ordering at the interface, inferred from Andreev reflection measurements [22]. Nevertheless, due to the comparable superconducting and magnetic critical fields of $NbSe_2$ and MBT, respectively, disentangling the magnetic behavior at the interface remains challenging. As such, a deeper understanding of the magnetic proximity effect in these systems is still lacking.

In this work, we fabricated NbN/MBT heterostructures by combining mechanical exfoliation of MBT single crystals and superconducting NbN thin films growth. Through the insertion of a 2-nm-thick Ti buffer layer, high-quality heterointerfaces were achieved. The interfacial differential resistance ($\mathrm{d}V/\mathrm{d}I$–I) spectra reveal three sets of additional critical current peaks, which are corresponding to the proximity-induced interfacial superconductivity. The magnetic field dependencies of these critical currents reveal modulation by magnetic phase transitions in the MBT layer. Additionally, hysteresis observed in the low-field regime of interfacial magnetoresistance (MR) curves suggests proximity-induced spin polarization at the interface. Our work demonstrates the coexistence of magnetism and superconductivity in a hybrid van der Waals crystal and thin film system, establishing a novel platform for investigating emergent quantum states, including including topological superconductivity and possibly Majorana zero modes.

2 Results and Discussion

2.1 Characterization of the NbN/$MnBi_2Te_4$ heterostructure

Figure 1**a** shows an optical micrograph of the device with the transport measurement layout. To characterize the interfacial properties, we fabricated a mesa [36] and combined it with a nonlocal measurement configuration, as illustrated schematically in Fig. 1**b**. In this setup, current is applied from the top electrode of the NbN mesa to one side of the underlying MBT, while the voltage is measured between the mesa and the opposite side of the MBT. As a result, the measured voltage includes contributions from both the NbN layer and the NbN/MBT interface. In particular, for in-plane angular-dependent magnetoresistance MR measurements, the magnetic field (B) is applied within the ab-plane of the sample. As a result, the Lorentz force acts within the plane and does not produce a transverse deflection of carriers out of the film, rendering the orbital contribution to the magnetoresistance negligible.

The quality of the interface plays a critical role in determining the transport properties of magnetic/superconducting heterostructures. To ensure minimal disorder and high interface integrity, we employed an *in situ* fabrication technique that integrates MBT crystal cleaving and NbN thin-film deposition. Details of the fabrication process are provided in the Supplementary Information. As shown in Fig. 1**c**, scanning transmission electron microscopy (STEM) combined with energy-dispersive X-ray spectroscopy (EDX) confirms the formation of a sharp, high-quality interface between the NbN layer and the MBT crystal.

The transport properties of the NbN/MBT heterostructure were systematically investigated using three distinct measurement configurations, as illustrated in Figs. 2**a**, 2**e**, and 2**i**. By applying current and measuring voltage at different locations, we were able to independently probe the transport characteristics of the interface, the MBT layer, and the NbN layer. Figures 2**b**, 2**f**, and 2**j** show the temperature-dependent resistance (R–T) curves corresponding to the interface, MBT, and NbN, respectively. Two distinct transitions are observed in the interfacial R–T curve (Fig. 2**b**) at approximately 10.8 K and 24.4 K. These transitions correspond to the superconducting critical temperature (T_c) of NbN and the Néel temperature (T_N) of MBT, as indicated in Figs. 2**j** and 2**f**, respectively. Below T_c, a resistance upturn is observed with decreasing temperature in the interfacial curve. This feature is attributed to enhanced Andreev reflection (AR) processes occurring at the NbN/MBT interface.

Figures 2**c**, 2**g**, and 2**k** show the out-of-plane MR curves of the interface, MBT, and NbN layers, respectively, measured at 2 K. On the interfacial MR curve (Fig. 2**c**), two sets of kinks are observed at $B = \pm 3$ T and ± 8 T. Given that the out-of-plane upper critical field of NbN far exceeds 16 T [37], these features are attributed to the spin-flop transition field (B_flop) and the magnetic saturation field (B_s) of MBT [38, 29, 30], as further supported by the MBT MR response in Fig. 2**g**. In addition, a small hysteresis loop appears near zero field in the interfacial MR curve, which will be discussed in more detail later. We note that Fig. 2**c** shows a single magnetic field sweep direction; full hysteresis loops confirming the coercive field and remanent resistance are provided in Fig. 7**b**.

To characterize the proximity-induced superconducting states, we performed I–V measurements for all three configurations. Figures 2**d**, 2**h**, and 2**l** show the differential resistance spectra ($\mathrm{d}V/\mathrm{d}I$) as a function of bias current I at 2 K for the interface, the MBT layer, and the NbN layer, respectively. In the interfacial spectrum (Fig. 2**d**), in addition to the AR peak appearing near zero current, three additional sets of peaks emerge at $I = \pm 0.95$ mA, ± 1.20 mA, and ± 2.10 mA, labeled as I_c^0, I_c^1, and I_c^2, respectively. Based on the intermediate magnitudes and field/temperature dependencies of these features, we associate I_c^1 and I_c^2 with the Ti buffer and the suppressed NbN interface region, respectively, and I_c^0 with the MBT layer. For comparison, the critical current of the bare NbN layer is about 5.8 mA, as shown in Fig. 2**l** and labeled I_c^3, significantly higher than those observed in the interfacial configuration. This further supports the interpretation that the lower critical currents originate from proximity-induced superconductivity. Additionally, the suppression of zero-bias conductance (AR peak) is consistent with our previous observations in NbSe$_2$/MBT heterostructures [22]. Note, however that while the suppression of zero-bias conductance is qualitatively consistent with ferromagnetic alignment along the c-axis, direct magnetization or spin-resolved measurements would be needed to confirm the interfacial spin texture.

2.2 Differential resistance spectra of the NbN/MnBi$_2$Te$_4$ heterostructure

The color map of the interfacial differential resistance spectra as functions of bias current and temperature is shown in Fig. 3**a**. Several characteristic contour lines, labeled as I_c^0, I_c^1, I_c^2, and I_c^3, appear symmetrically on both the positive and negative current sides of the map. These features correspond to different superconducting regions within the heterostructure, as discussed previously. As the temperature increases, the zero-bias AR peak gradually diminishes and eventually vanishes at the superconducting critical temperature of $\approx$6 K, indicating the suppression of proximity-induced superconductivity. Figure 3**b** displays line profiles of the differential resistance spectra at selected temperatures. The dashed lines trace the temperature evolution of the critical currents I_c^0, I_c^1, I_c^2, and I_c^3.

Figure 4**a** shows the out-of-plane field-dependent color map of the interfacial differential resistance spectra measured at 2 K. For comparison, the corresponding in-plane field-dependent color map is shown in Fig. 4**c**. In both cases, the zero-bias AR peak gradually diminishes as the magnetic field increases, reflecting the suppression of proximity-induced superconductivity. However, the critical currents exhibit markedly different behaviors under the two field orientations. Under in-plane magnetic fields, the contour lines corresponding to I_c^0, I_c^1, and I_c^2 decrease monotonically with increasing field. In contrast, the out-of-plane data reveal an anomalous kink near $B = 3$ T, coinciding with the spin-flop transition field of

MBT, indicating an interplay between interfacial superconductivity and magnetic ordering. Figures 4**b** and 4**d** show the line profiles of the differential resistance spectra at selected out-of-plane and in-plane fields, respectively. The dashed lines trace the field evolution of I_c^0, I_c^1, and I_c^2. Note that the critical current of bulk NbN (≈5.8 mA at 2 K) lies beyond the current measurement range and is thus not visible in these plots.

Considering the proximity effect at the NbN/MBT interface, as illustrated in Fig. 5**a**, superconducting correlations (i.e., the pair amplitude associated with the NbN order parameter) extend across the interface into the MBT layer, inducing a proximity superconducting state near the heterointerface [39, 40, 35]. In addition, the presence of spin polarization at the interface can suppress superconductivity via exchange interactions [41]. As a result, multiple superconducting energy gaps are expected at the interface: the bulk superconducting gap (Δ_3), the interface-suppressed gap (Δ_2), and the proximity-induced gaps (Δ_1, Δ_0). Although the absence of a zero-resistance state in the interfacial region precludes direct extraction of these gap magnitudes, Bardeen-Cooper-Schrieffer (BCS) theory provides a proportional relationship between the superconducting energy gap and the critical current [42]. Therefore, by analyzing the temperature and magnetic field dependence of the critical currents, we can gain insight into the nature of the interfacial superconducting state. Figure 5**b** presents the temperature-dependent critical currents I_c^0, I_c^1, I_c^2, and I_c^3, corresponding to the proximity-induced superconductivity in the MBT layer, the Ti buffer layer, the suppressed NbN region at the interface, and the bulk NbN layer, respectively. In the BCS framework, the critical current $I_c(T)$ is expected to follow the temperature dependence $I_c(T) \propto [1-(T/T_c)^2]^{3/2}$ near T_c, reflecting the behavior of the superconducting gap and superfluid density. All four sets of critical currents broadly follow this BCS-like temperature dependence, suggesting that the proximity-induced superconducting states may be governed by conventional BCS theory. While these results are consistent with conventional BCS superconductivity, we also observe nonmonotonic magnetic field responses and anisotropic peak broadening in angular-dependent measurements. These could, in principle, also arise from spin-orbit coupling effects or emergent triplet components. However, more phase-sensitive probes will be required to determine the pairing symmetry unambiguously. In contrast to their monotonic suppression under in-plane magnetic fields (Fig. 5**d**), the critical currents exhibit anomalous kinks near $B = 3$ T when subjected to out-of-plane fields (Fig. 5**c**). This anomaly coincides with the spin-flop transition of MBT, wherein the magnetic moments reorient from out-of-plane to in-plane. While the data suggest a possible interplay with spin–orbit coupling, the temperature dependence of the critical currents remains consistent with BCS theory, and no direct evidence of spin-triplet pairing is observed. Further experiments will be required to clarify whether unconventional components contribute to the induced superconductivity.

Figure 6 presents the angular-dependent differential resistance spectra. During the measurements, the external magnetic field B was rotated within the ab-plane, as illustrated in Fig. 6**a**, where θ denotes the angle between B and the x-axis. Figures 6**b**-6**e** show color maps of the differential resistance spectra measured at $B = 1$, 4, 7, and 9 T, respectively. As the magnetic field is increased, the critical currents systematically shift to lower values, and the width of the differential resistance peaks broadens progressively. Notably, at high fields, the peak widths exhibit a pronounced two-fold rotational symmetry with respect to θ, while the peak positions remain largely angle-independent. These results suggest anisotropic suppression of the superconducting correlations under in-plane rotation of the magnetic field. However, the angle-invariant critical current positions imply a preserved isotropy in the dominant pairing amplitude. To definitively determine the underlying superconducting pairing symmetry, more direct, phase-sensitive measurements will be required.

2.3 Magnetic transport properties of the NbN/MnBi$_2$Te$_4$ heterostructure

MBT is a well-established A-type antiferromagnet, exhibiting ferromagnetic intralayer coupling and antiferromagnetic interlayer coupling between Mn magnetic moments. When NbN is brought into contact with MBT, spin polarization is induced at the interface via the magnetic proximity effect, resulting in a ferromagnetic character right at the heterointerface, as illustrated in Fig. 7**a**. To probe this interfacial spin polarization, we performed MR measurements across the interface at various temperatures, with the magnetic field applied along the c-axis. The results are shown in Fig. 7**b**. Unlike the MR response of bulk MBT [43], pronounced hysteresis loops emerge in the low-field region of the interfacial MR curves, indicating the onset of interfacial ferromagnetism. An abrupt enhancement of MR is observed near 10 K, which we attribute to flux-flow resistance in NbN's superconducting transition regime, where even small magnetic fields can significantly affect the resistance. Figure 7**c** shows the extracted coercive field (B_c, upper panel) and hysteresis amplitude (ΔR, lower panel) as functions of temperature. Notably, B_c remains well below the spin-flop transition field B_flop ($\approx$3 T) of MBT. Both B_c and ΔR decrease with increasing temperature and vanish around $T \approx 25$ K, which closely matches the Néel temperature T_N ($\approx$24.4 K) of MBT. This temperature dependence strongly supports the interpretation that the observed interfacial magnetism arises from the magnetic proximity effect. These results therefore demonstrate the coexistence of superconductivity and spin polarization at the NbN/MBT heterointerface, highlighting the effectiveness of proximity engineering in realizing hybrid quantum states.

3 Conclusion

In summary, we have demonstrated the coexistence of superconductivity and magnetism at the interface between a conventional superconductor (NbN) and a van der Waals magnetic topological insulator (MBT), realized in a carefully engineered heterostructure. High interface quality, enabled by *in vacuo* exfoliation and Ti buffer-layer protection during NbN deposition, is crucial for preserving the intrinsic magnetic and electronic properties of the constituent layers. Transport measurements reveal interfacial behavior distinct from that of either constituent: the R–T and MR curves exhibit signatures attributable to both the superconducting NbN and antiferromagnetic MBT, confirming electronic coupling between the two materials. Differential resistance spectra show three distinct sets of critical currents (I_c^0, I_c^1, I_c^2), which we associate with proximity-induced superconducting correlations in the MBT layer, the Ti buffer layer, and the interface-suppressed region of NbN, respectively. These findings indicate that superconducting correlations originating in the NbN layer extend across the interface and mediate coherent transport in the adjacent magnetic material. Notably, the critical currents are modulated by the spin-flop transition of the MBT layer, providing direct evidence of coupling between the superconducting proximity effect and the magnetic order parameter. In addition, low-field magnetoresistance measurements reveal a clear hysteresis loop localized to the interface, consistent with proximity-induced spin polarization. Despite these manifestations of nontrivial interfacial coupling, the extracted critical currents follow BCS-like temperature dependence, and no unambiguous signatures of unconventional pairing are observed. These results suggest that while the induced superconducting state remains conventional in nature, the interface provides a robust and tunable platform for exploring hybrid quantum phases. Compared to earlier studies of NbN/MBT heterostructures [34, 35], our work demonstrates enhanced interfacial integrity, multichannel superconductivity, magnetic hysteresis, and field-tunable transport features, made possible by precise interface engineering. The approach presented here thus offers a powerful platform for future investigations of topological superconductivity, magnetically modulated proximity effects, and potential Majorana physics in superconductor-magnet hybrid systems.

4 Experimental Section

Crystal growth

Single crystals of $MnBi_2Te_4$ (MBT) were grown using a solid-state reaction method. A stoichiometric mixture of MnTe and Bi_2Te_3 powders, with a molar ratio of 1:5, was placed into an alumina crucible and sealed in a quartz ampoule under vacuum. The ampoule was heated to 700 °C for 30 hours, then slowly cooled to 590 °C at a rate of 5 °C/h. Afterward, the furnace was allowed to cool naturally to room temperature. High-quality MBT crystals were obtained. To confirm phase purity and crystallinity, crystals were ground and analyzed using powder X-ray diffraction (XRD), yielding results consistent with previous reports.

Fabrication of the NbN/$MnBi_2Te_4$ heterostructure

NbN/MBT heterostructures were fabricated by combining mechanical exfoliation of the 2D material with thin-film deposition techniques, as detailed in Note 1 (Supporting Information). To ensure high-quality interfaces, the entire assembly process was conducted under high-vacuum conditions. First, MBT flakes were mechanically exfoliated from bulk crystals and transferred onto pre-cleaned SiO_2 (300 nm)/Si substrates using a custom-built high-vacuum transfer system. The samples were then transferred into a magnetron sputtering chamber, using a vacuum transfer system, for deposition of a 2 nm Ti buffer layer followed by a 40 nm NbN layer. The Ti layer enhances adhesion at the NbN/MBT interface and protects the MBT surface from damage during the high-power sputtering of NbN (200 W), thereby preserving interfacial integrity [44, 45].

Subsequently, the heterostructures were patterned into short strips via electron-beam lithography and reactive ion etching. A 50-nm-thick SiO_2 layer was deposited on the remaining substrate areas to prevent side contact. Finally, Ti (10 nm)/Au (100 nm) electrodes were fabricated using standard photolithography and metal lift-off processes, as illustrated in Fig. 1**b**.

Electrical transport measurements

Electrical transport measurements of the NbN/MBT devices were carried out using a Physical Property Measurement System (PPMS; Quantum Design). A constant DC current was applied between two superconducting electrodes using a Keithley 2182 nanovoltmeter, and the voltage between another pair of superconducting electrodes was measured using a Keithley 2400 source meter. The interfacial resistance was calculated as $R = V/I$. Current–voltage (I–V) characteristics of the devices were also measured using the source and nanovoltmeters in a standard two-terminal configuration.

Supporting Information

Supporting Information is available from the Wiley Online Library or from the author.

Acknowledgments

Y. Wang and P. Dong contributed equally to this work.

This research was supported in part by the Ministry of Science and Technology (MOST) of China (No. 2022YFA1603903), the National Natural Science Foundation of China (Grants Nos. 12434005, 12104302, 12104303), the Natural Science Foundation of Shanghai (Grants Nos. 25ZR1402374, 25ZR1402368, and 25ZR1401252), the Science and Technology Commission of Shanghai Municipality, the Shanghai Leading Talent Program of the Eastern Talent Plan, and the Double First-Class Initiative Fund of ShanghaiTech University.

References

[1] M. B. Maple, *Appl. Phys.* **1976**, *9*, 3 179.

[2] A. B. Karki, V. O. Garlea, R. Custelcean, S. Stadler, E. W. Plummer, R. Jin, *Proc. Natl. Acad. Sci.* **2013**, *110*, 23 9283.

[3] C. Pfleiderer, *Rev. Mod. Phys.* **2009**, *81*, 4 1551.

[4] N. P. Armitage, P. Fournier, R. L. Greene, *Rev. Mod. Phys.* **2010**, *82*, 3 2421.

[5] P. Dai, *Rev. Mod. Phys.* **2015**, *87*, 3 855.

[6] N. D. Mathur, F. M. Grosche, S. R. Julian, I. R. Walker, D. M. Freye, R. K. W. Haselwimmer, G. G. Lonzarich, *Nature* **1998**, *394*, 6688 39.

[7] F. Onufrieva, P. Pfeuty, *Phys. Rev. Lett.* **2012**, *109*, 25 257001.

[8] A. Chubukov **2012**, *3*, Volume 3, 2012 57.

[9] I. M. Hayes, D. S. Wei, T. Metz, J. Zhang, Y. S. Eo, S. Ran, S. R. Saha, J. Collini, N. P. Butch, D. F. Agterberg, A. Kapitulnik, J. Paglione, *Science* **2021**, *373*, 6556 797.

[10] S. S. Saxena, P. Agarwal, K. Ahilan, F. M. Grosche, R. K. W. Haselwimmer, M. J. Steiner, E. Pugh, I. R. Walker, S. R. Julian, P. Monthoux, G. G. Lonzarich, A. Huxley, I. Sheikin, D. Braithwaite, J. Flouquet, *Nature* **2000**, *406*, 6796 587.

[11] N. Tateiwa, Y. Haga, E. Yamamoto, *Phys. Rev. Lett.* **2018**, *121*, 23 237001.

[12] S. Ran, C. Eckberg, Q.-P. Ding, Y. Furukawa, T. Metz, S. R. Saha, I. L. Liu, M. Zic, H. Kim, J. Paglione, N. P. Butch, *Science* **2019**, *365*, 6454 684.

[13] D. S. Wei, D. Saykin, O. Y. Miller, S. Ran, S. R. Saha, D. F. Agterberg, J. Schmalian, N. P. Butch, J. Paglione, A. Kapitulnik, *Phys. Rev. B* **2022**, *105*, 2 024521.

[14] G. Qiu, H.-Y. Yang, L. Hu, H. Zhang, C.-Y. Chen, Y. Lyu, C. Eckberg, P. Deng, S. Krylyuk, A. V. Davydov, R. Zhang, K. L. Wang, *Nat. Commun.* **2023**, *14*, 1 6691.

[15] M. Iavarone, S. A. Moore, J. Fedor, S. T. Ciocys, G. Karapetrov, J. Pearson, V. Novosad, S. D. Bader, *Nat. Commun.* **2014**, *5*, 1 4766.

[16] J. Linder, J. W. A. Robinson, *Nat. Phys.* **2015**, *11*, 4 307.

[17] Y. Zhu, A. Pal, M. G. Blamire, Z. H. Barber, *Nat. Mater.* **2017**, *16*, 2 195.

[18] G. Hu, C. Wang, J. Lu, Y. Zhu, C. Xi, X. Ma, Y. Yang, Y. Zhang, S. Wang, M. Gu, J. Zhang, Y. Lu, P. Cui, G. Chen, W. Zhu, B. Xiang, Z. Zhang, *ACS Nano* **2025**, *19*, 5 5709.

[19] H. T. Yi, X. Yao, D. Jain, Y.-T. Chan, A.-H. Chen, M. Brahlek, K. Kisslinger, K. Du, M.-G. Han, Y. Zhu, W. Wu, S.-W. Cheong, S. Oh, *Adv. Funct. Mater.* **2025**, *35*, 25 2418259.

[20] L. Ai, E. Zhang, J. Yang, X. Xie, Y. Yang, Z. Jia, Y. Zhang, S. Liu, Z. Li, P. Leng, X. Cao, X. Sun, T. Zhang, X. Kou, Z. Han, F. Xiu, S. Dong, *Nat. Commun.* **2021**, *12*, 1 6580.

[21] K. Flensberg, F. von Oppen, A. Stern, *Nat. Rev. Mater.* **2021**, *6*, 10 944.

[22] P. Dong, X. Hou, J. He, Y. Zhang, Y. Ding, X. Zeng, J. Wang, Y. Wu, K. Watanabe, T. Taniguchi, W. Xia, Y. Guo, Y. Chen, X. Zhou, W. Li, J. Li, *Phys. Rev. B* **2024**, *109* L140503.

[23] L. Fu, C. L. Kane, *Phys. Rev. Lett.* **2008**, *100*, 9 096407.

[24] K. Ishida, H. Mukuda, Y. Kitaoka, K. Asayama, Z. Q. Mao, Y. Mori, Y. Maeno, *Nature* **1998**, *396*, 6712 658.

[25] R. Balian, N. R. Werthamer, *Phys. Rev.* **1963**, *131*, 4 1553.

[26] D. Zhang, M. Shi, T. Zhu, D. Xing, H. Zhang, J. Wang, *Phys. Rev. Lett.* **2019**, *122*, 20.

[27] J. Li, Y. Li, S. Du, Z. Wang, B.-L. Gu, S.-C. Zhang, K. He, W. Duan, Y. Xu, *Sci. Adv.* **2019**, *5*, 6 eaaw5685.

[28] Y. Deng, Y. Yu, M. Z. Shi, Z. Guo, Z. Xu, J. Wang, X. H. Chen, Y. Zhang, *Science* **2020**, *367*, 6480 895.

[29] S. Yang, X. Xu, Y. Zhu, R. Niu, C. Xu, Y. Peng, X. Cheng, X. Jia, Y. Huang, X. Xu, J. Lu, Y. Ye, *Phys. Rev. X* **2021**, *11*, 1 011003.

[30] Z. Lian, Y. Wang, Y. Wang, W.-H. Dong, Y. Feng, Z. Dong, M. Ma, S. Yang, L. Xu, Y. Li, B. Fu, Y. Li, W. Jiang, Y. Xu, C. Liu, J. Zhang, Y. Wang, *Nature* **2025**, *641*, 8061 70.

[31] J.-X. Qiu, B. Ghosh, J. Schütte-Engel, T. Qian, M. Smith, Y.-T. Yao, J. Ahn, Y.-F. Liu, A. Gao, C. Tzschaschel, H. Li, I. Petrides, D. Bérubé, T. Dinh, T. Huang, O. Liebman, E. M. Been, J. M. Blawat, K. Watanabe, T. Taniguchi, K. C. Fong, H. Lin, P. P. Orth, P. Narang, C. Felser, T.-R. Chang, R. McDonald, R. J. McQueeney, A. Bansil, I. Martin, N. Ni, Q. Ma, D. J. E. Marsh, A. Vishwanath, S.-Y. Xu, *Nature* **2025**, *641*, 8061 62.

[32] A. I. Buzdin, *Rev. Mod. Phys.* **2005**, *77*, 3 935.

[33] M. K. Hope, M. Amundsen, D. Suri, J. S. Moodera, A. Kamra, *Phys. Rev. B* **2021**, *104* 184512.

[34] J. Chen, W. Xu, Z. Tan, Z. Pan, P. Zhu, Z.-M. Liao, D. Yu, *Nano Lett.* **2022**, *22*, 16 6484.

[35] W.-Z. Xu, C.-G. Chu, Z.-C. Pan, J.-J. Chen, A.-Q. Wang, Z.-B. Tan, P.-F. Zhu, X.-G. Ye, D.-P. Yu, Z.-M. Liao, *Phys. Rev. B* **2022**, *105*, 18 184515.

[36] J. Li, P. J. Pereira, J. Yuan, Y.-Y. Lv, M.-P. Jiang, D. Lu, Z.-Q. Lin, Y.-J. Liu, J.-F. Wang, L. Li, X. Ke, G. Van Tendeloo, M.-Y. Li, H.-L. Feng, T. Hatano, H.-B. Wang, P.-H. Wu, K. Yamaura, E. Takayama-Muromachi, J. Vanacken, L. F. Chibotaru, V. V. Moshchalkov, *Nat. Commun.* **2017**, *8*, 1 1880.

[37] A. Semenov, B. Günther, U. Böttger, H. W. Hübers, H. Bartolf, A. Engel, A. Schilling, K. Ilin, M. Siegel, R. Schneider, D. Gerthsen, N. A. Gippius, *Phys. Rev. B* **2009**, *80*, 5 054510.

[38] J. Cui, M. Shi, H. Wang, F. Yu, T. Wu, X. Luo, J. Ying, X. Chen, *Phys. Rev. B* **2019**, *99*, 15.

[39] V. Mourik, K. Zuo, S. M. Frolov, S. R. Plissard, E. P. A. M. Bakkers, L. P. Kouwenhoven, *Science* **2012**, *336*, 6084 1003.

[40] H. Kim, A. Palacio-Morales, T. Posske, L. Rózsa, K. Palotás, L. Szunyogh, M. Thorwart, R. Wiesendanger, *Sci. Adv.* **2018**, *4*, 5 eaar5251.

[41] M. Eschrig, T. Löfwander, *Nat. Phys.* **2008**, *4*, 2 138.

[42] J. Bardeen, *Rev. Mod. Phys.* **1962**, *34*, 4 667.

[43] M. Z. Shi, B. Lei, C. S. Zhu, D. H. Ma, J. H. Cui, Z. L. Sun, J. J. Ying, X. H. Chen, *Phys. Rev. B* **2019**, *100*, 15 155144.

[44] D. H. Olson, K. M. Freedy, S. J. McDonnell, P. E. Hopkins, *Appl. Phys. Lett.* **2018**, *112*, 17.

[45] Y. Wang, B. Fu, Y. Wang, Z. Lian, S. Yang, Y. Li, L. Xu, Z. Gao, X. Yang, W. Wang, W. Jiang, J. Zhang, Y. Wang, C. Liu, *Nat. Commun.* **2025**, *16*, 1 1727.

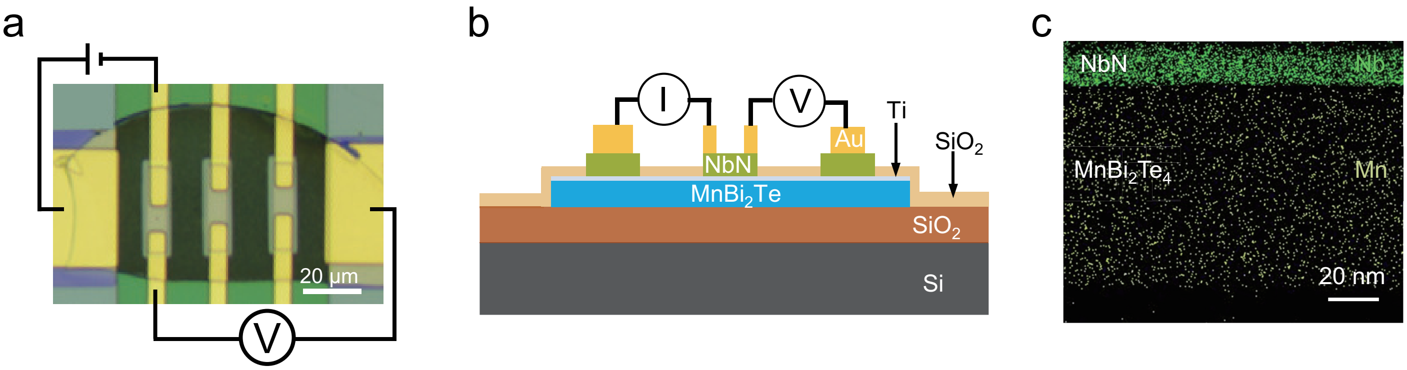

Figure 1: **Sample geometry and interface of the NbN/MnBi$_2$Te$_4$ heterostructure. a** Optical microscope image of the fabricated NbN/MBT device. **b** Cross-sectional schematic of the heterostructure showing the layer sequence. **c** Elemental mapping of Nb and Mn obtained via STEM-EDX, confirming the elemental composition and sharpness of the interfacial region.

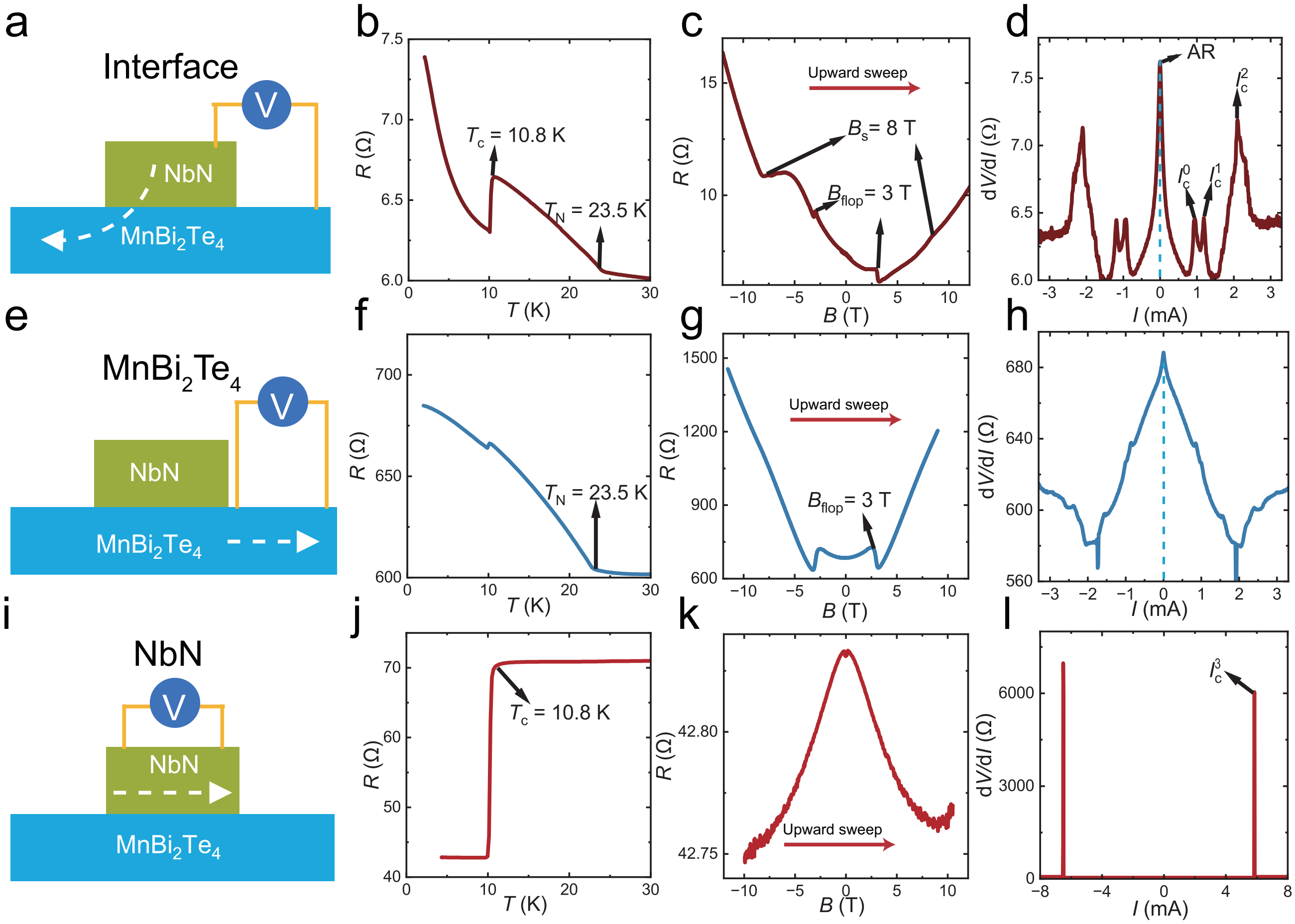

Figure 2: **Transport properties of the NbN/MnBi$_2$Te$_4$ heterostructure. a, e, i** Measurement schematics for the interface, MBT, and NbN layers, and **b, f, j** respective temperature-dependent resistances measured under zero magnetic field. In the R–T curve of the interface (**b**), two distinct transitions are observed: the superconducting transition of NbN at $T_c = 10.8$ K and the antiferromagnetic transition of MBT at $T_N = 23.5$ K. **c, g, k** Out-of-plane magnetoresistance curves at 2 K for the interface, MBT, and NbN layers. In **c** and **g**, the spin-flop transition field (B_{flop}) and the saturation field (B_s) of MBT are clearly identified. **d, h, l** Differential resistance (dV/dI) versus bias current I at 2 K for the interface, MBT, and NbN layers. In **d**, the zero-bias peak labeled AR is attributed to Andreev reflection, while additional peaks at higher bias currents, labeled I_c^0, I_c^1, and I_c^2, correspond to the critical currents of proximity-induced superconducting states at the interface, and I_c^3 to that of the NbN film itself.

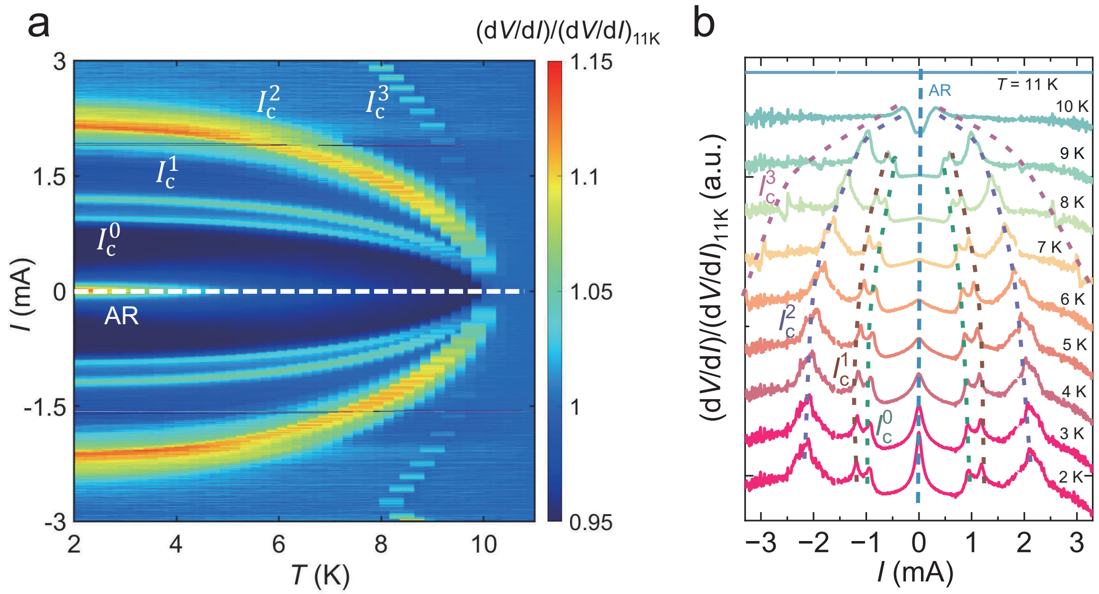

Figure 3: **Temperature-dependent differential resistance spectra of the NbN/MnBi$_2$Te$_4$ heterostructure. a** Color map of dV/dI as a function of bias current I and temperature. **b** Line profiles of normalized differential resistance spectra at selected temperatures. Dashed lines in **b** trace the evolution of critical currents I_c^0, I_c^1, I_c^2, and I_c^3 as a function of temperature.

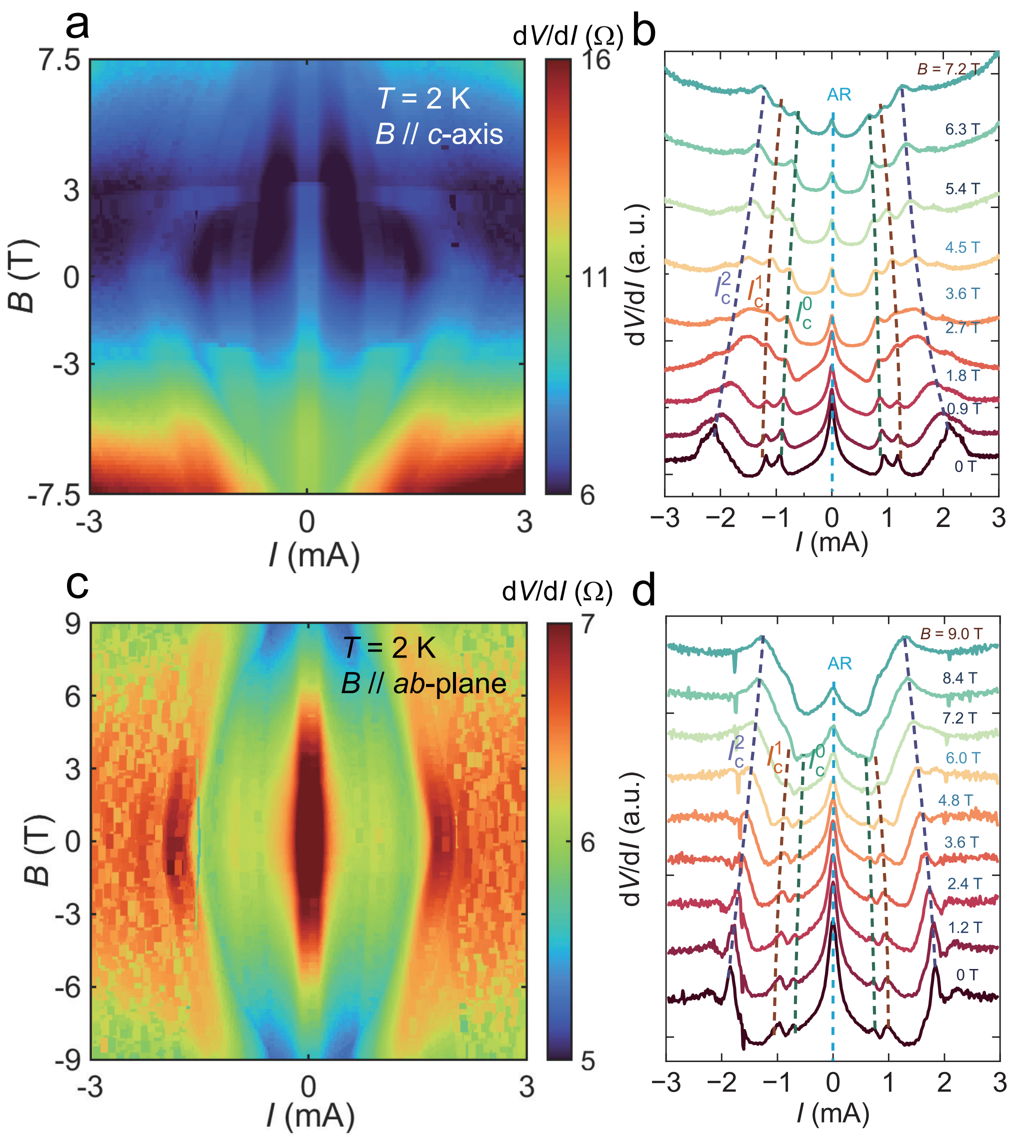

Figure 4: **Field-dependent differential resistance spectra of the NbN/MnBi$_2$Te$_4$ heterostructure. a, c** Color maps of differential resistance as a function of out-of-plane (**a**) and in-plane (**c**) magnetic field. **b, d** Line profiles of differential resistance spectra at selected out-of-plane (**b**) and in-plane (**d**) magnetic fields. Dashed lines in **b** and **d** trace the evolution of critical currents I_c^0, I_c^1, and I_c^2 as a function of applied field. The critical current of intrinsic NbN, I_c^3, exceeds the measurement range and is therefore not visible in these spectra.

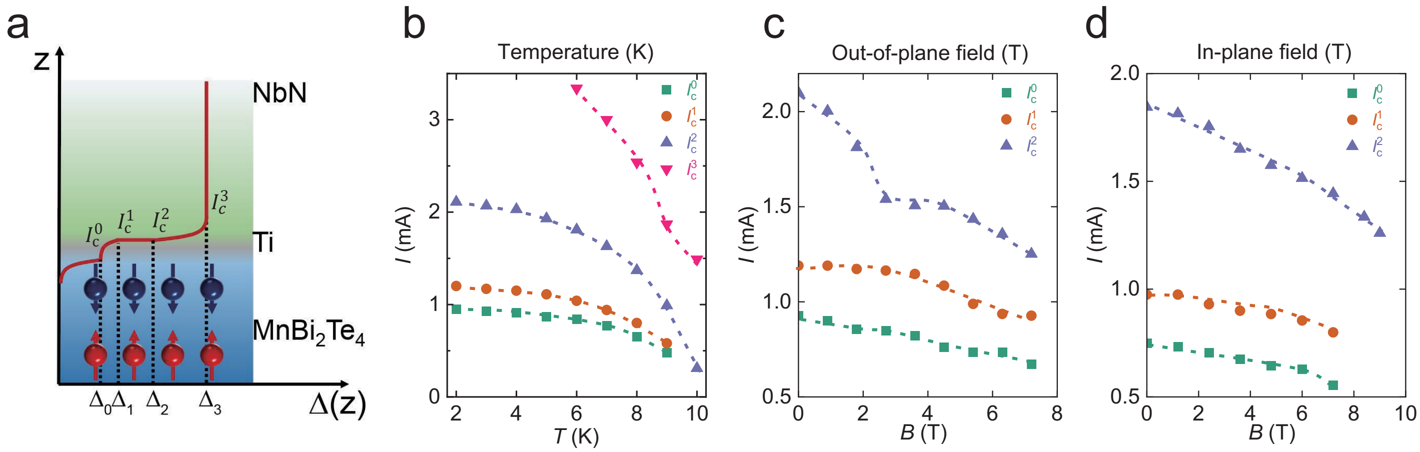

Figure 5: **Temperature- and field-dependent critical currents.** **a** Schematic illustration of proximity-induced superconductivity across the NbN/$\mathrm{MnBi_2Te_4}$ interface. **b** Extracted critical currents I_c^0, I_c^1, I_c^2, and I_c^3 as a function of temperature. **c, d** Critical currents as a function of out-of-plane (**c**) and in-plane (**d**) magnetic field. Dashed lines in **b**, **c** and **d** serve as guides to the eye.

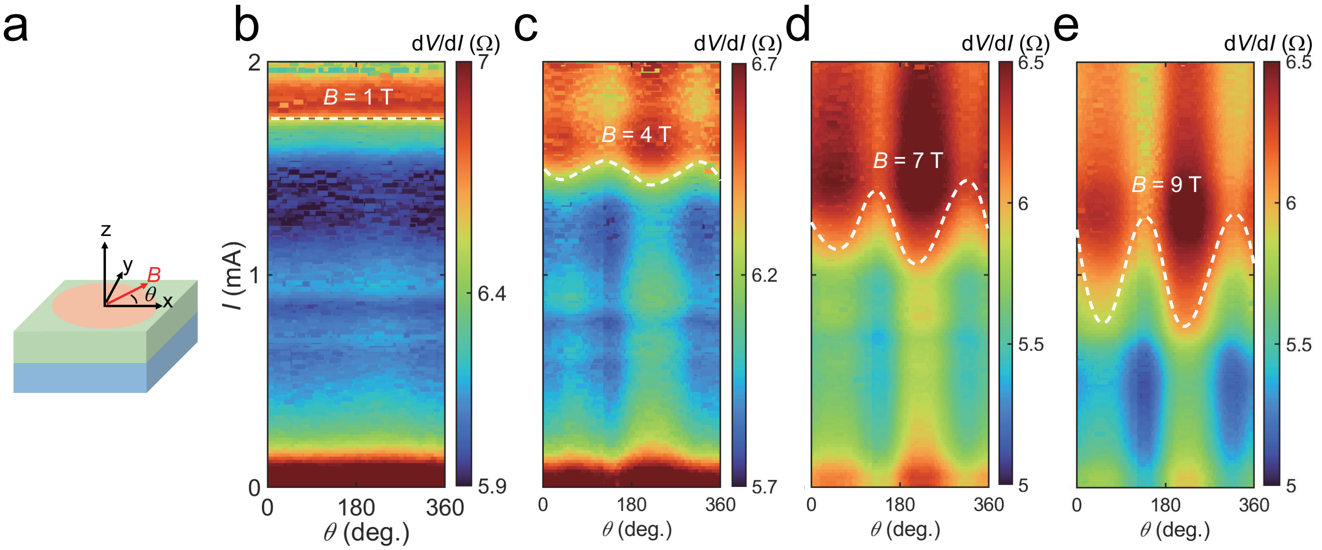

Figure 6: **Angular-dependent differential resistance spectra.** **a** Schematic of the azimuthal field rotation, where θ denotes the angle between the applied magnetic field and the x-axis within the sample plane. **b-e** Differential resistance color maps as functions of bias current and in-plane angle θ under out-of-plane magnetic fields of 1 T (**b**), 4 T (**c**), 7 T (**d**), and 9 T (**e**). Data were acquired at $T = 2\,\mathrm{K}$.

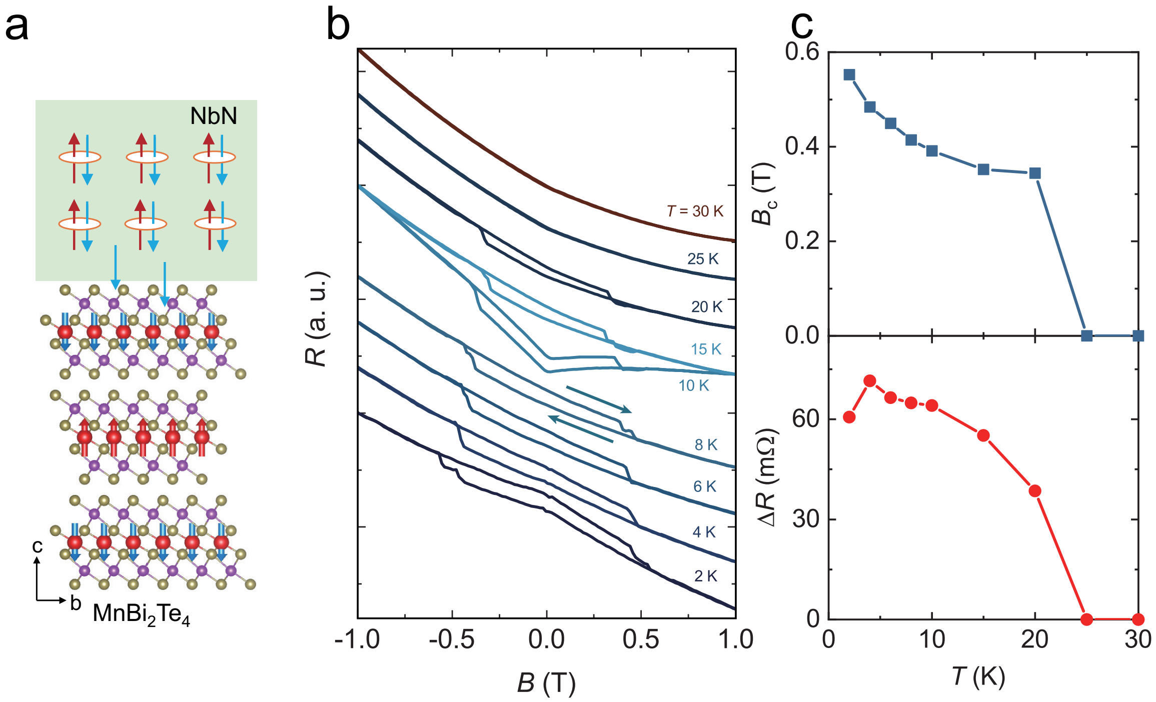

Figure 7: **Magnetic transport properties of the NbN/MnBi$_2$Te$_4$ interface.** **a** Schematic illustration of the spin structure in the NbN/MBT heterostructure. The NbN layer exhibits no spin polarization, while the MBT layer hosts A-type antiferromagnetism, with intralayer ferromagnetic and interlayer antiferromagnetic coupling. Proximity-induced spin polarization arises at the interface. **b** Out-of-plane MR curves at various temperatures. The magnetic field scan was performed in a cyclic sequence: -1 T → +1 T → -1T. Hysteretic behavior emerges below T_{N}. **c** Temperature dependence of the extracted coercive field (B_{c}, upper panel) and hysteresis amplitude (ΔR, lower panel).